Continuous dynamic recrystallization in an Al–Li–Mg–Sc alloy during equal-channel angular extrusion

R. Kaibyshev [a,*], K. Shipilova [a], F. Musin [a], Y. Motohashi [b]

[a] *Institute for Metals Superplasticity Problems RAS, Khalturina Street 39, Ufa 450001, Russia*
[b] *Ibaraki University, Research Center of Superplasticity, Nakanarusawa-cho, 4-12-1 Hitachi, Ibaraki 316-8511, Japan*

Abstract

An Al–Li–Mg–Sc alloy with an initial grain size of ~60 μm was processed by equal-channel angular extrusion (ECAE) at 300 °C up to a total strain of 12. Transmission electron microscopy (TEM) and orientation imaging microscopy (OIM) were employed to establish the mechanism of grain refinement. It was found that new ultrafine grains evolved by a strain-induced continuous process, which is termed continuous dynamic recrystallization (CDRX). At $\varepsilon \sim 1$, a well-defined subgrain structure had developed. Upon further straining the average mis-orientation of deformation-induced boundaries increased; low-angle boundaries (LAB) gradually converted into true high-angle boundaries (≥15°) (HAB). At $\varepsilon \sim 4$, arrays of boundaries with low and high angle mis-orientations were observed. At $\varepsilon \sim 12$, a structure dominated by HAB with an average grain size of ~0.9 μm was formed. This size is roughly similar to that for subgrains developed at preceding strains. It was shown that CDRX occurs homogeneously; the formation of new grains takes place both along initial boundaries and within interiors of original grains as well.

Keywords: Equal-channel angular extrusion; Continuous dynamic recrystallization; Ultrafine grain structure; Aluminum–lithium alloy

1. Introduction

There is currently significant commercial interest in the development of Al–Li–Mg alloys with an ultra-fine grain structure for structural applications [1]. The formation of a uniform ultra-fine recrystallized micro-structure provides high service properties and enhanced workability of these alloys. In the unrecrystallized condition, these alloys exhibit poor toughness and marginal plasticity at ambient temperature due to extensive localization of plastic deformation [1]. Recent works have demonstrated that substantial grain refinement in Al–Li–Mg alloys can be achieved through the introduction of intense plastic deformation via equal-channel angular extrusion (ECAE) [2,3]. However, no attention has been given in these studies to the microstructure evolution resulting in the grain refinement. Examination of the deformed state during severe deformation of Al–Li alloys seems to have not yet been carried out.

The general features of the microstructure evolution during ECAE processing of aluminum alloys have been recently examined [4–13]. The most popular method for examining grain boundaries produced during ECAE processing, the selected-area electron diffraction (SAED) technique, yields only qualitative information [5–8]. To date, orientation imaging microscopy (OIM) has rarely been employed to examine the influence of ECAE strain on the mis-orientation distribution in aluminum alloys [4,10–12].

Prangnell and co-workers used high-resolution electron back scattered diffraction (EBSD) technique to examine the microstructure evolution in aluminum alloys containing micron-scale second-phase particles [9,10]. These authors suggested that the grain refinement in aluminum alloys under ECAE at low temperatures occurs by the extension and compression of initial grain boundaries followed by the discontinuous formation of transverse high-angle boundaries (HABs)

* Corresponding author. Tel.: +7 3472 253856; fax: +7 3472 253856.
E-mail address: rustam@anrb.ru (R. Kaibyshev).

[9,10]. It was assumed that the latter provides a major fraction of the resulting HABs [9].

Other workers have emphasized the role of continuous dynamic recrystallization (CDRX) [14,15]. In particular, this mechanism has been proposed to explain the grain refinement in an Al–Mn alloy under ECAE [5]. In CDRX, new grains result from the gradual increase in mis-orientation between subgrains during plastic deformation [14,15]. The presence of nano-scale dispersoids restricts the mobility of deformation-induced boundaries [14] and enables the operation of this mechanism of grain refinement during severe plastic deformation.

The objective of the present work is to study the microstructural evolution in an Al–Li–Mg–Sc alloy processed using ECAE at 300 °C. OIM is employed to characterize the deformation-induced boundaries with the intent of establishing the mechanism of grain refinement.

2. Experimental

The 1421 aluminum alloy with a chemical composition of Al–4.1%Mg–2.0%Li–0.16%Sc–0.08%Zr (wt.%), denoted as 1421 Al, was manufactured by direct chill casting followed by solution treatment at 460 °C for 24 h. The alloy was cut into cylinders 20 mm in diameter and 100 mm in length.

The ECAE processing was carried out in air using an isothermal die with a circular internal cross-section. The channel had an L-shaped configuration with angles $\Phi \sim 90^\circ$ and $\psi \sim 1^\circ$ (as defined by Iwahashi et al. [7]). Deformation through these angles produces a strain of ~1 on each passage through the die [6,8]. The samples were extruded to several strains (namely: 1, 2, 4, 8 and 12 passes) at 300 °C (~0.7 T_m, where T_m is the melting point). Route A in which the specimen is removed from the die and the extrusion is repeated without any rotation of the sample [4–6,16] was used. The shearing characteristics for this processing route in a tabular form were clearly presented in Fig. 6 of work [16]. The repetitive extrusion was continuously conducted with intermediate holdings in a furnace at 300 °C for ~10 min. Total time, at which the specimen was held at deformation temperature during ECAE processing, was ~15 min per each extrusion pass. It was shown in a previous work [3] that grain growth occurs only for $T > 400$ °C in 1421 Al with an initial submicrocrystalline structure and, therefore, interpass static annealing is not expected to effect the microstructure. The specimens were water quenched after ECAE processing. The extrusion velocity was about 2 mm/s. Calculation of the strain rate during a single ECAE pass is a very difficult task due to the strong effect of friction. In addition, there exists a dependence of strain rate on position within the workpiece [17–19]. Assuming that the ratio between extrusion velocity and strain rate in the present experiment is similar to that obtained in [19] by FEM calculations, one can assume that the strain rate in the plane of intersection of the two channels is about $10^{-1}\ s^{-1}$.

Following ECAE, samples were sliced from the central area of the billets, the slicing plane was parallel to the extrusion direction and contained the extrusion direction (ED) and the transverse extrusion direction (ET). That is, the deformed structure was characterized at the centre of the Y plane (Fig. 1 of [16]). Discs 3 mm in diameter were cut from these slices and then were ground to a thickness of ~0.25 mm. For EBSD analysis these discs were electro-polished to give a strain-free surface. EBSD orientation maps were recorded using a Jeol JSM-840 SEM fitted with automated HKL-EBSD pattern collection system with a spatial resolution of ~500 nm and an angular resolution of ~1° provided by Oxford Instruments Ltd. The examining area was automatically scanned in 0.5 μm steps. In the data presented, HABs were defined as being greater than or equal to 15° in mis-orientation and low-angle boundaries (LAB) as having a mis-orientation of less than 15° but being greater than 3°. LABs with mis-orientation less than 3° were not taken into account. HABs and LABs are depicted in OIM maps as thick and thin lines, respectively. Terms 'grain' and 'subgrains' are used for definition of crystallites, which are entirely delimited by HABs and LABs, respectively [15]. The '(sub)grains' are crystallite which are bounded partly by LABs and partly by HABs. The volume fraction of ultrafine grains was deemed to be the 'recrystallized' fraction. The 'crystallite size' is defined as the mean separation of all boundaries (HABs + LABs) [20]. The density of boundaries, γ, was determined by the ratio between the length of the HABs and LABs and the area of the OIM map.

For TEM analysis, similar discs were electro-polished to perforation with a Tenupol-3 twinjet polishing unit using a standard 75%CH_3COOH + 25%HNO_3 solution at −30 °C and 20 V. The thin foils were examined using a Jeol-2000EX TEM with a double-tilt stage at an accelerating potential of 160 kV. SAED patterns were taken from regions 12.3 μm in diameter. Representative photomicrographs were obtained to determine the subgrain or grain sizes using the mean linear-intercept method.

The density of lattice dislocations was estimated using the intercept relationship [21]:

$$\rho = \frac{1}{t}\left(\frac{n_1}{L_1} + \frac{n_2}{L_2}\right), \tag{1}$$

where n_1 and n_2 are the numbers of intercepts on sets of orthogonal lines of total lengths L_1 and L_2 on the normal image, and t the foil thickness, which was evaluated by analyzing grain boundary extinction contours [21]. Details of energy dispersive X-ray analysis (EDS) of thin foils, which was carried out to identify second phase particles, were reported in [22].

3. Experimental results

3.1. Microstructure before deformation

The initial microstructure of the 1421 Al after solution treatment consisted of equiaxed grains with an average grain size of about 60 μm (Fig. 1a). No subgrain structure was observed within the grains. The density of randomly distributed dislocations was $\sim 10^{11}$ m^{-2}. Two types of second-phase particles were found. The one type were particles with a plate-like morphology with dimensions of approximately 1 μm in longitudinal and 0.5 μm in transverse directions. These coarse particles were identified by TEM analysis as Al_2LiMg (designated as S-phase) [23]. The other type were equiaxed particles with a size ranging from 20 to 60 nm, which were identified as $Al_3(Sc, Zr)$ dispersoids (Fig. 1b). These nano-scale dispersoids exhibited the specific 'bean-coffee' contrast suggesting their coherent origin (Fig. 1b).

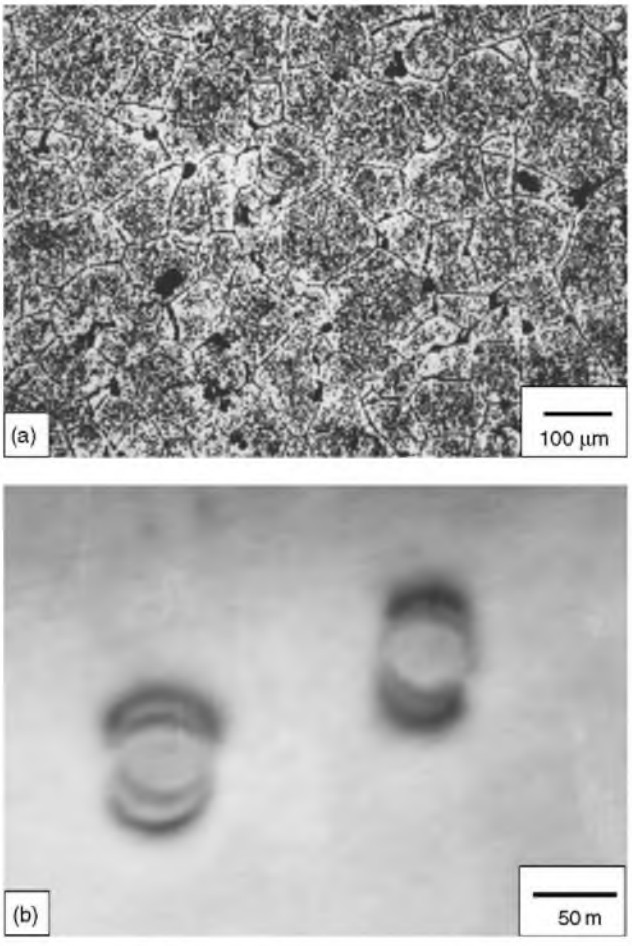

Fig. 1. Initial microstructure of 1421 Al after solution treatment: (a) optical micrograph; (b) TEM micrograph.

3.2. Microstructure evolution during severe deformation at 300° C

3.2.1. One ECAE pass

Fig. 2 represents the microstructures and associated SAED patterns after pressing. It is seen that a well-defined subgrain structure is formed after first passage (Fig. 2a, b). LABs are sharp and consist of well-ordered dislocation arrays suggestive of a subgrain structure (Fig. 2a, b) [14]. No boundaries consisting of tangled arrays of dislocations [14] were found. The deformed structure is inhomogeneous; two structural components could be distinguished. One component was a band-like structure consisting of elongated subgrains aligned along the shear direction (Fig. 2a). The other component was made up of essentially equiaxed (sub)grains (Fig. 2b). The density of 'free' dislocations within the subgrains is $\sim 10^{13}$ m^{-2}. These subgrains are ~1.5 μm in length along the shear direction and ~0.8 μm in thickness. The average size of the equiaxed (sub)grains is ~0.8 μm. The coherent $Al_3(Sc, Zr)$ precipitates effectively pin sub-boundaries. It is worth noting that no remarkable difference was seen between the deformed structure near the coarse particles of the S-phase and areas remote from the particles (Fig. 2b).

Figs. 3a and 4a show OIM maps and the distribution of mis-orientation angles after the first pass through the die. Three-dimensional mixed arrays of LABs and HABs evolved within old grains, which were favorable oriented for multiple slip on the $\{1\,1\,1\}\ \langle 1\,1\,0\rangle$ systems (Fig. 3a). The (sub)grains are dominating here, and new equiaxed grains can be also found. The (sub)grains and new grains appear homogeneously both within grain interiors and along original boundaries. However, the density of deformation-induced boundaries in the vicinity of the initial boundaries is slightly higher than that within the grain interiors. This suggests a moderate local strain gradient near the old grain boundaries. Only separate LABs are formed within the initial grains in which the $\{1\,1\,1\}$ planes lie in the Y plane (Fig. 3a) [16]; three-dimensional arrays of LABs could be detected near the old boundaries here. In general, the population of LABs is about 70% (Fig. 4a). Therefore, in the 1421 Al a significant portion of HABs is achieved and new recrystallized grains evolved even after $\varepsilon \sim 1$.

3.2.2. Two ECAE passes

After $\varepsilon \sim 2$, most of the (sub)grains exhibit equiaxed shape (Fig. 2c). A notably increased dislocation density ($\rho \sim 4 \times 10^{13}$ m^{-2}) appears within the elongated subgrains, and a low dislocation density ($\rho \sim 5 \times 10^{12}$ m^{-2}) was found within the equiaxed (sub)grains. The second pass leads to the evolution of well-defined arrays of deformation-induced boundaries within the interiors of almost all old grains, which are highly elongated in the shear direction (Fig. 3b). A number of new fine grains appear along the initial grain boundaries thus making up a mantle surrounding the initial grains (Fig. 3b). It is apparent that the average mis-orientation of the deformation-induced boundaries is higher in the vicinity

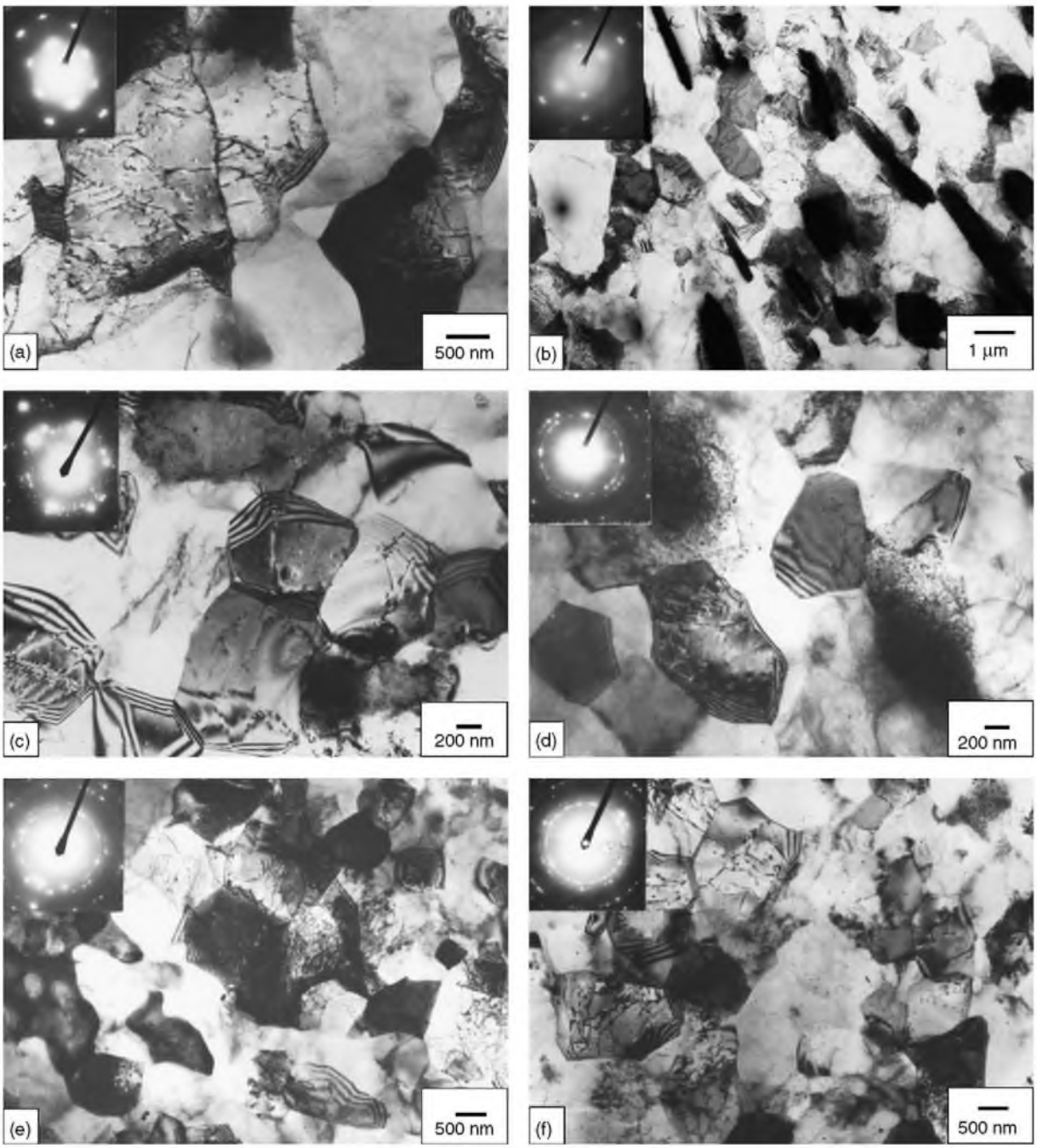

Fig. 2. Typical microstructure and associated SAED patterns for: (a, b) $\varepsilon \sim 1$; (c) $\varepsilon \sim 2$; (d) $\varepsilon \sim 4$; (e) $\varepsilon \sim 8$; (f) $\varepsilon \sim 12$.

of the old grain boundaries than that in the core of the grains. After second pass through the die the fraction of LABs decreases to 60%. (Fig. 4b).

3.2.3. *Four ECAE passes*

Pressing to a strain of four results in a partially recrystallized structure (Figs. 2d and 3c). A fully recrystallized structure was formed within separate initial grains. Recovered subgrains and (sub)grains could be observed within the other original grains (Figs. 2d and 3c). In general, HABs dominate in the deformed structure (Figs. 2d, 3c and 4c). The average mis-orientation is 28°; the proportion of HABs is ~71%. (Fig. 4c). The fraction of recrystallized grains is ~43%. Thus, a high fraction of submicrometer scale grains is developed in 1421 Al after a relatively moderate strain. A well-defined peak associated with LABs is observed (Fig. 4c) in the histogram of mis-orientation distribution.

3.2.4. *Eight and twelve ECAE passes*

Processing to higher strains leads to the formation of a fully recrystallized structure; most of deformation-induced

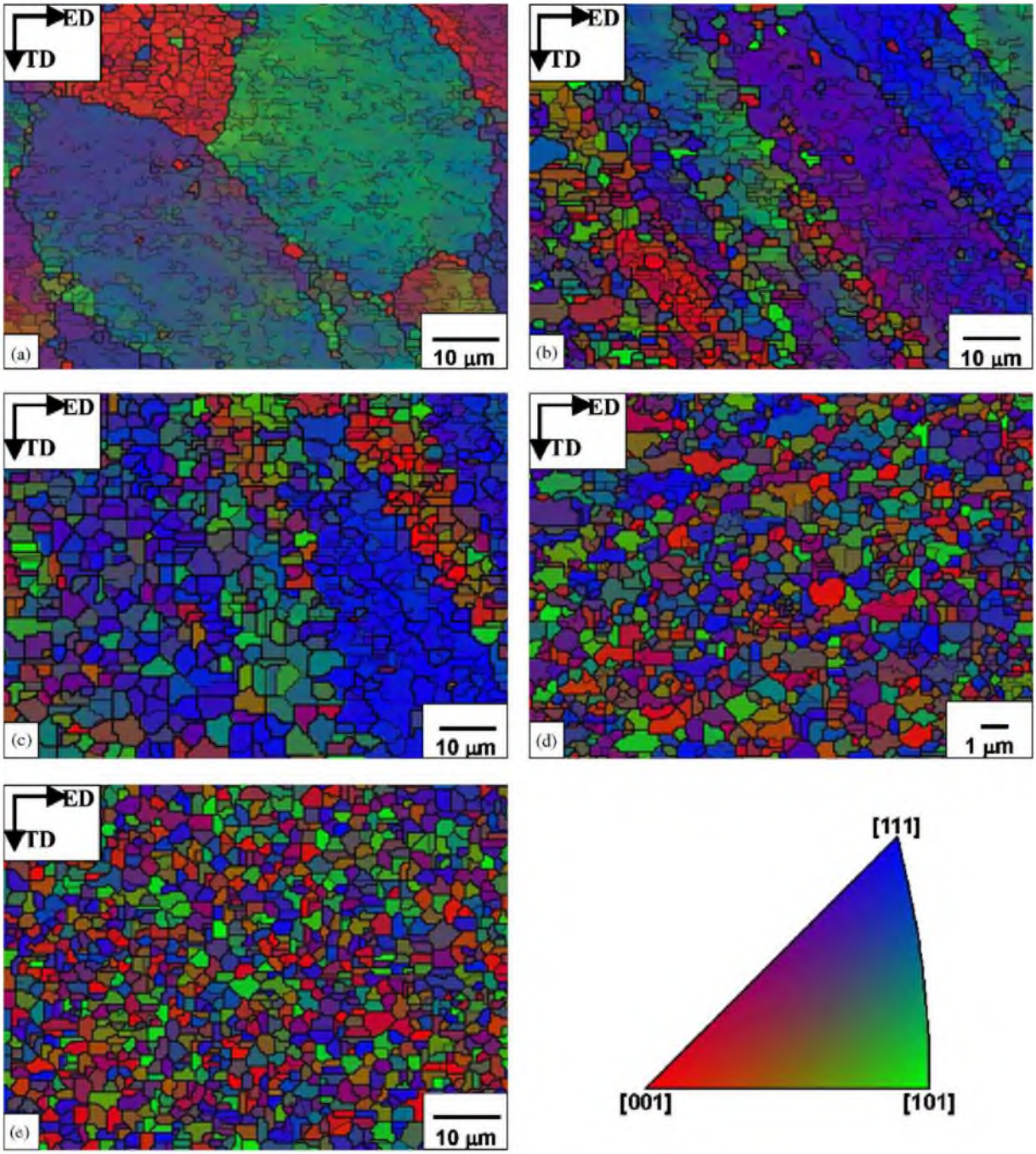

Fig. 3. Fine-scale EBSD maps for: (a) $\varepsilon \sim 1$; (b) $\varepsilon \sim 2$; (c) $\varepsilon \sim 4$; (d) $\varepsilon \sim 8$; (e) $\varepsilon \sim 12$.

boundaries have high-angle origin (Figs. 2e, f and 3d, e). At $\varepsilon \sim 8$, the volume fraction of grains is about 50%. (Fig. 3d). The population of HABs is ~90%. (Fig. 4d). A low density of lattice dislocations ($\rho \sim 6 \times 10^{12}\ m^{-2}$) within the new grains was found (Fig. 2e). LABs are observed within relatively coarse new grains (Fig. 3d). Two peaks associated with LABs and HABs can be distinguished in the mis-orientation histograms (Fig. 4d).

After $\varepsilon \sim 12$, the uniformity of the recrystallized structure increases (Figs. 2f and 3e). Most of the deformation-induced boundaries are high-angle in mis-orientation and the recrystallized grains exhibit an equiaxed shape (Fig. 3e). A relatively low density of lattice dislocations ($\sim 8 \times 10^{12}\ m^{-2}$) is present within the grains and no LABs were found within the interiors of the fine recrystallized grains (Figs. 2f and 3e). An increased recrystallized fraction (~95%.) suggests that grain refinement is complete at this strain. It is apparent that in the strain interval 8–12 a slight increase in proportion of HABs leads to the transformation of (sub)grains occupying about 40% of the overall volume at $\varepsilon \sim 8$ into grains at $\varepsilon \sim 12$.

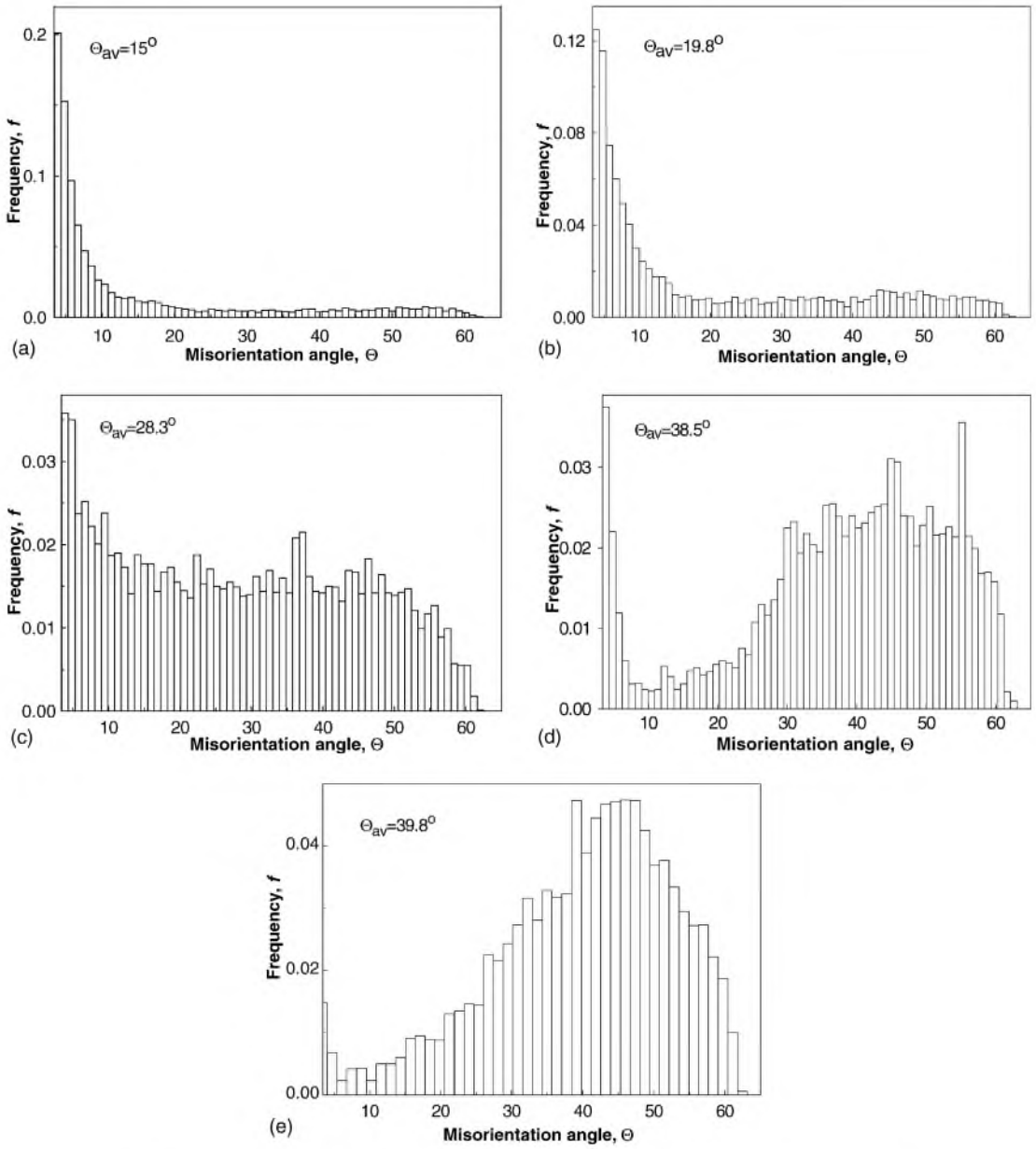

Fig. 4. Mis-orientation distribution during ECAE for: (a) $\varepsilon \sim 1$; (b) $\varepsilon \sim 2$; (c) $\varepsilon \sim 4$; (d) $\varepsilon \sim 8$; (e) $\varepsilon \sim 12$.

3.3. Parameters of the deformed microstructure as a function of strain

Effect of ECAE on the structural parameters is summarized in Fig. 5, which shows the effect of strain on the crystallite size, d, the average mis-orientation between boundaries, θ, the proportion of HABs (in overall numbers of deformation-induced boundaries), the fraction of recrystallized grains, V, and the density of boundaries, γ, having low-angle and high-angle origin. These measurements were averaged from several OIM maps at each strain level. In the strain interval 1–4 the crystallite size rapidly decreases owing to an increasing fraction of equiaxed (sub)grains and a decreasing population of elongated subgrains; the longitudinal size of the elongated subgrains tends to decrease with strain due to the formation of transverse LABs (Figs. 3a–c). As a result, the grain aspect ratio (AR), defined as the ratio of the grain dimension in the shear direction to that in the transverse direction decreases from 1.8 at $\varepsilon \sim 1$ to 1.3 at $\varepsilon \sim 4$ (Fig. 5a). Upon further ECAE processing the average crystallite size tends to grow slightly suggesting slow migration of HABs; the AR decreased to 1.2 at $\varepsilon \sim 12$.

The data in Fig. 5b clearly demonstrate the high rate of grain refinement in 1421 Al. A high fraction of HABs appears after $\varepsilon \sim 1$ and the average mis-orientation is 15°. In the strain interval 1–4 the mis-orientation data can be approximated

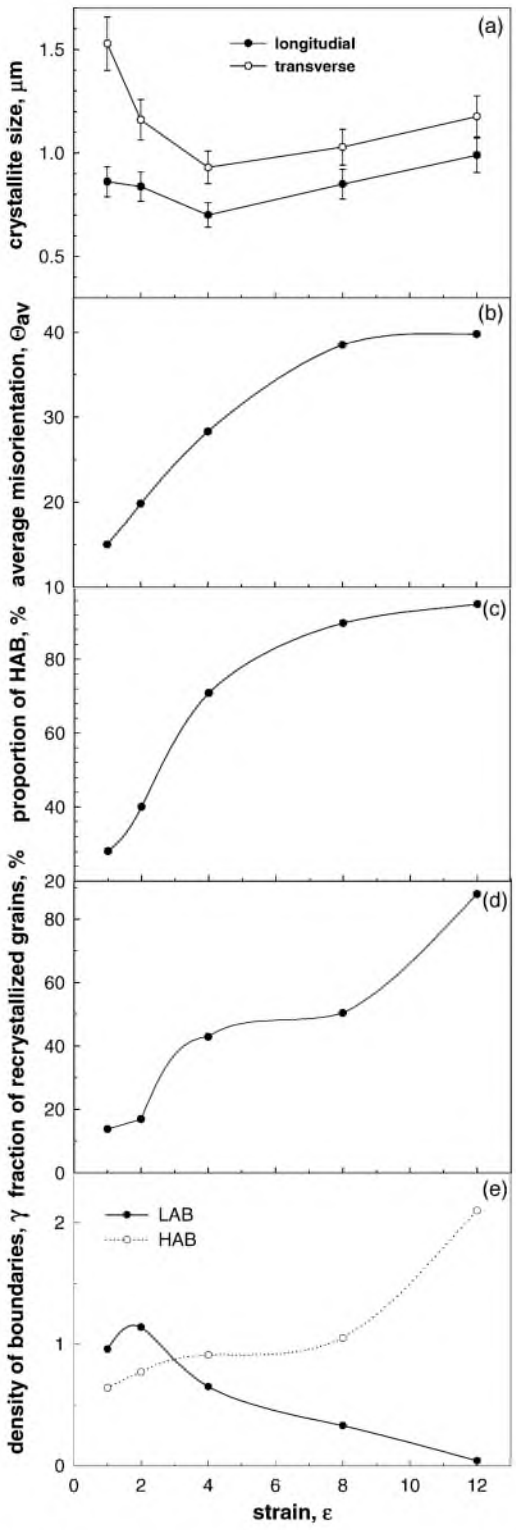

Fig. 5. Effect of strain on the crystallite size, d, (a) average mis-orientation of deformation-induced grain boundaries, θ_{av}, (b) population of HABs, (c) fraction of recrystallized grains and (d) density of deformation-induced boundaries, γ, having low-angle and high-angle origin (e).

by a linear function of cumulated strain, that is $\Delta\theta \propto 5^\circ \times \varepsilon$. Similarly high values of the rate of increase of mis-orientation have been reported for CDRX in Al–Li–Cu–Mg alloy under conditions of superplastic deformation [24]. At $\varepsilon \sim 4$, the average mis-orientation is close to 30°. This value is equivalent to the saturation value for copper and stainless steel [25]. In the present case, the saturation value of the average mis-orientation is about 40° (Fig. 5b), a value similar to that obtained for a random distribution of polycrystalline grains, 40.7° [26]. Therefore, it is apparent that a fully recrystallized structure with a mis-orientation distribution equivalent to a random assembly is formed in 1421 Al at $\varepsilon \sim 8$. Increasing strain leads to increased uniformity of the ultra-fine grained structure.

Fig. 5e shows that an increase in the density of LABs takes place with increasing strain for $\varepsilon \leq 2$; further straining results in a gradual decrease in the density of LABs. The density of HABs increases with deformation for all strains. Inspection of these data shows that the formation of LABs persistently occurs under ECAE. As a result, a peak associated with LABs is observed on the mis-orientation histograms at all strains (Fig. 4). LABs continuously transform into HABs providing a continuous increase in the proportion of HABs (Fig. 5c). An increase in the density of LABs at moderate strains is associated with the formation of transverse sub-boundaries that provides the transition from the unrecrystallized structure consisting of separate LABs to the three-dimensional arrays of LABs. It is seen that an increase in the density of deformation-induced boundaries is the main process of structural evolution at $\varepsilon \leq 2$. At $\varepsilon \geq 4$, the main process is a gradual conversion of LABs into HABs. This is why, at $\varepsilon \leq 2$, the formation of recrystallized grains occurs at a low rate, and at higher strains, this process is highly accelerated (Fig. 5c). It is worth noting that the present strain dependence of HAB density could not have been derived from geometrical processes taking into account the extremely high decrease in the thickness of initial grains [14,27]. The experimental rate of the formation of deformation-induced boundaries is far too high for the geometrical process. Therefore, geometric dynamic recrystallization [14,27] is not a mechanism of grain refinement in 1421 Al at 300 °C.

3.4. Microtexture evolution

The textures are given as {1 1 1} pole figures as a function of strain in Fig. 6. In the strain interval 1–4 these are typical of an fcc shear texture [28,29]; the intensity tends to increase with strain. At $\varepsilon > 4$, the strain increase results in texture randomization (Fig. 6d and e). Therefore, texture strengthening is associated with a transition from a subgrain structure to a grain structure, and texture randomization is attributed to severe plastic deformation in the presence of a fine grained structure. Notably, at $\varepsilon > 2$, the texture evolution can be affected by the progressive wrapping of the billet under ECAE with increasing strain [9,31].

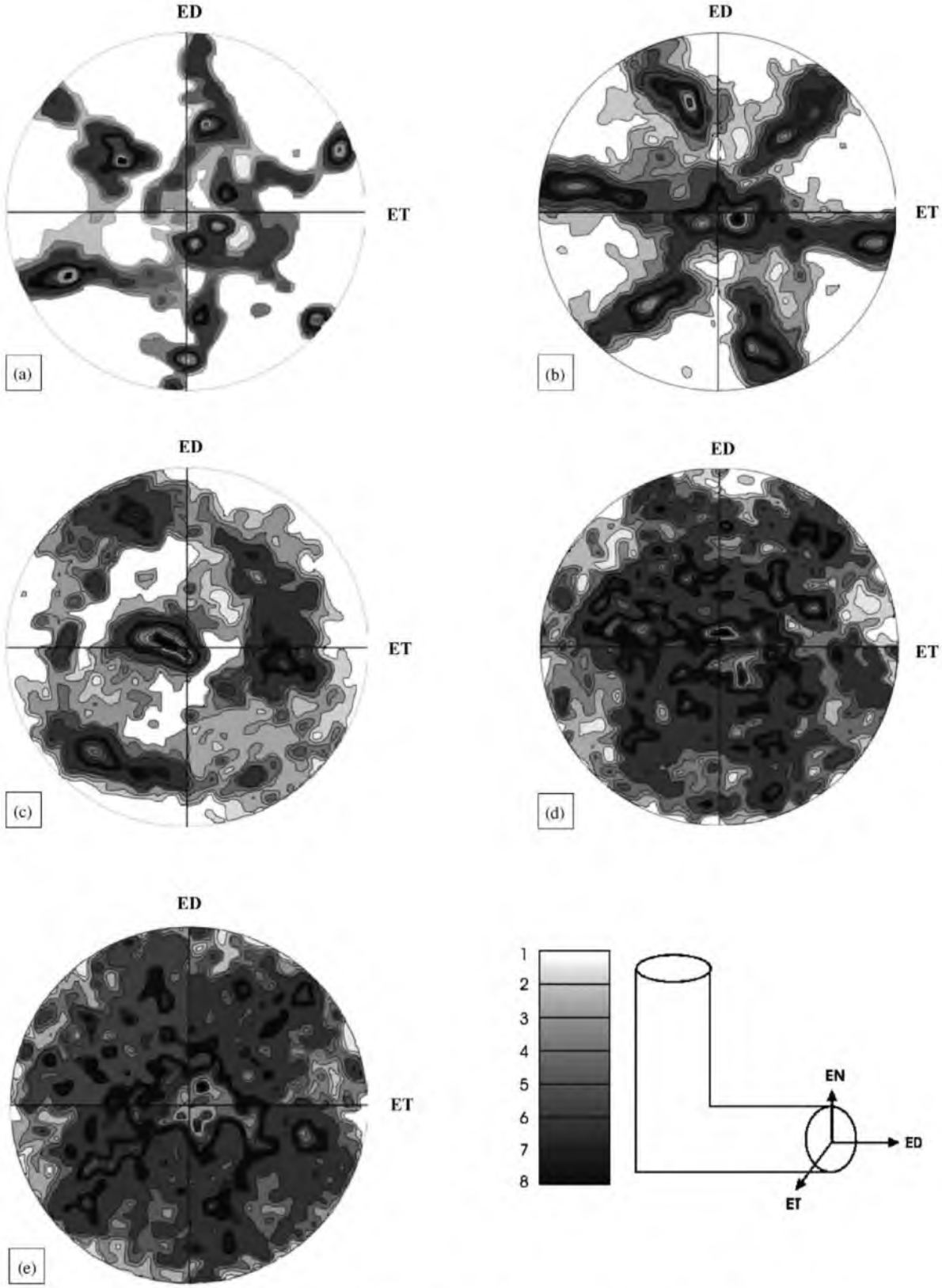

Fig. 6. Evolution of microtexture in the 1421 Al under ECAE: (a) $\varepsilon \sim 1$; (b) $\varepsilon \sim 2$; (c) $\varepsilon \sim 4$; (d) $\varepsilon \sim 8$; (e) $\varepsilon \sim 12$.

It is worth noting that at $\varepsilon \sim 2$ the texture is similar to that obtained at $\varepsilon \sim 7$ in torsion of low alloy aluminum [28] taking into account that the shear plane under ECAE processing is located at an angle of 45° to ED axis [16]. The formation of such type of texture was explained in work [28] in terms of rotation of subgrains away from the stable texture fiber resulting in a strong alignment of the rotation axes in the radial direction [28]. Therefore, one can assume that an extensive rotation of (sub)grains takes place within the 'ladder-like' structure [30] which forms in initial grains with orientation close to {1 1 1} (Fig. 3a, b) in 1421 Al under ECAE processing at $\varepsilon \leq 2$. It seems that this process provides increasing mis-orientation of deformation-induced boundaries in original grains in which the {1 1 1} planes lie at right angle to the shear plane.

4. Discussion

Inspection of experimental data shows that grain refinement in 1421Al occurs through a continuous strain-induced reaction, which has elsewhere been termed CDRX [19,25,32]. This mechanism of microstructure evolution during severe deformation in 1421 Al consists of two sequential processes:

(i) the formation of three-dimensional arrays of LABs;
(ii) the gradual transformation of LABs into HABs.

4.1. The formation of subgrain structure

LABs with a low mis-orientation (~1°) are continuously formed by dynamic recovery during deformation by rearrangement of accumulating lattice dislocations [14,19]. There exist two ways for the evolution of these LABs. First, the LABs can be involved in the process of CDRX resulting in the formation of a ultra-fine grained structure. Second, migration of LABs consisting of dislocations of opposite sign can result in their collision and elimination [33,34]. It is known that LAB with the mis-orientation close to 1° exhibit high mobility in pure aluminum and dilute aluminum alloys [14] which yields to their mutual annihilation [33]. However, in alloy 1421 the coherent $Al_3(Sc, Zr)$ dispersoids act as an effective pinning agent to hinder the migration of LABs thus stabilizing them [35]. As a result, the evolving sub-boundaries do not collapse; their density grows with strain for $\varepsilon \leq 2$, i.e. the first way of evolution of LABs dominates in 1421 Al.

It was recently shown [34,35] that LABs are formed at a high rate if they are located in the primary slip planes in the shear direction. The LABs aligned in the shear direction exhibit increased mis-orientation in comparison with transverse LABs [36] at low strains. It is apparent, that the formation of elongated subgrains at $\varepsilon \sim 1$ can be attributed to the easy formation of such LABs. Transverse LABs form within these elongated subgrains (Fig. 7a) by dislocation rearrangement. This provides the transformation of elongated

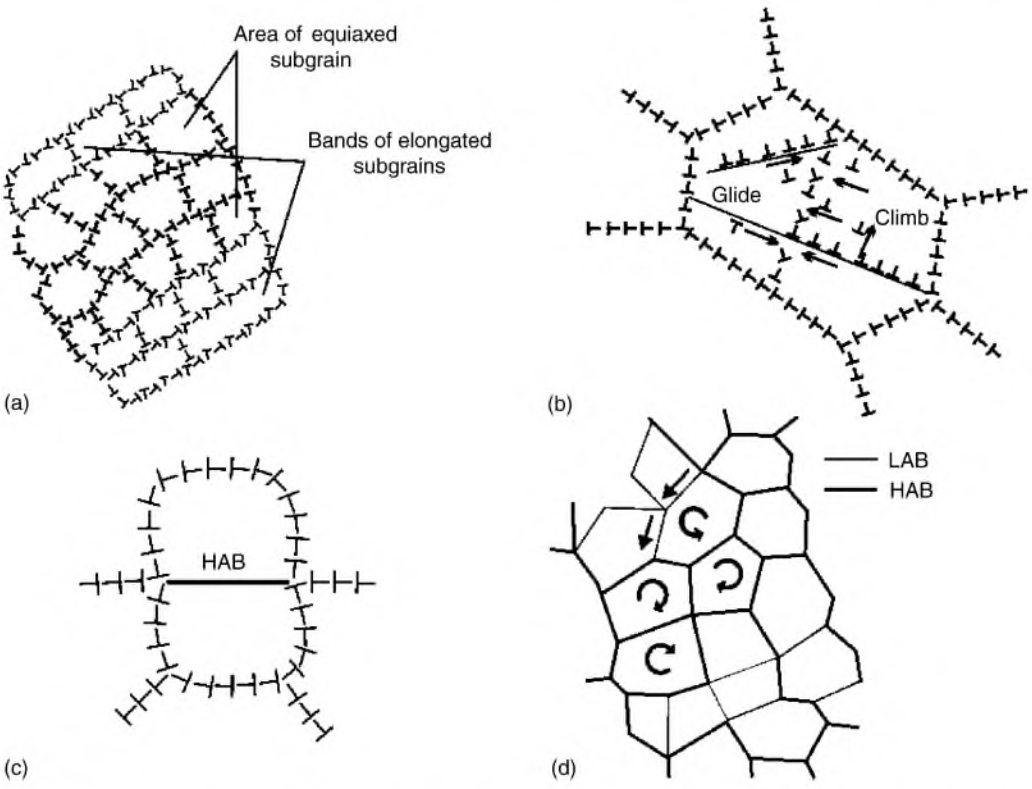

Fig. 7. Schematic representation of CDRX in the 1421 Al: (a) the formation of arrays of equiaxed subgrains alternating with areas of elongated subgrains; (b) interaction of low-angle boundaries with lattice dislocations resulting in progressive increase in their mis-orientation; (c) a nucleus in 3-D subgrain structure; (d) rotation of (sub)grains facilitates the transformation of low-angle boundaries into high-angle boundaries (HABs).

subgrains into subgrains with an essentially equiaxed shape and decreased lattice dislocation density. The rotation of subgrains within 'ladder-like' structure [30] provides increasing mis-orientation of transverse boundaries with strain.

A feature of CDRX in 1421 Al at 300 °C under ECAE is the uniform formation of a subgrain structure within individual grains. It seems that at this intermediate temperature, grain boundary sliding (GBS) along initial boundaries does not give significant contribution to total deformation. As a result, strain incompatibilities in the vicinity of initial boundaries associated with this process [14] are not so high; a moderate strain gradient arises within the initial grains due to GBS. The plate-like shape of the S-phase particles does not provide particle-stimulated nucleation [37] in 1421 Al.

4.2. Transformation of subgrain structure into recrystallized structure

It is obvious that at $\varepsilon > 2$, a decrease in density of LABs (Fig. 5e) occurs due to their conversion into HABs. The recrystallized grains persistently replace subgrains evolved at small passes through continuous transformation of their boundaries. Dislocation glide occurs within the subgrain interiors (Fig. 7b) [34]. Mobile dislocations move across subgrains and are trapped by sub-boundaries resulting in an increase in their mis-orientation (Fig. 7b). As a result, LABs eventually convert to true HABs. This is why a low dislocation density is observed within the interiors of submicron-scale (sub)grains. In addition, extensive rotation of subgrains in the plane of EBSD observation [28] provides increasing mis-orientation of LABs with strain within subgrains and (sub)grains with similar orientation (the 'ladder-like' structure; Fig. 3). These processes result in the formation of individual segments of HAB that appear not be related to original HABs [28] and can be considered as a proof for the occurrence of CDRX [19,28,32].

Initially the boundary between a crystallite and one of its neighbor acquires a high-angle mis-orientation. This (sub)grain being a small volume of relatively perfect material, which is at least partly bounded by a HAB (Fig. 7c), can be considered as a nucleus [38]. The transformation of a nucleus into a grain occurs by the conversion of all its LAB facets into HABs. In contrast with classic theory [14,38], the migration of this HAB into the recovered material is not important for the formation of recrystallized grains in 1421 Al under ECAE at 300 °C. It is apparent that a small increase in the crystallite size at $\varepsilon > 4$ can be attributed to the simple transition of triple junctions of LABs with contact angles of ~90° to HABs with triple junction angles of 120°. In the strain interval 4–8 the acceleration of transformation of LABs into HABs (Fig. 5c, e) resulting in extensive growth of the recrystallized fraction (Fig. 5d) can be caused by GBS along the isolated segments of HABs. McNelley and co-workers [39] suggested that GBS was not restricted to HAB segment but also occurred on adjacent LABs. Continuity between the sliding subgrain boundaries is achieved by the generation and absorption of dislocations [35]. It was recently shown [40,41] that GBS occurring along separate segments of HABs in partially recrystallized and layered structures is accommodated by the rotation of the LABs attached to them [35]. As a result, extensive (sub)grain rotation occurs in such a structure (Fig. 7d). This rotation highly accelerates the increase in the mis-orientation of LABs with strain (Fig. 7d) [41]. At $\varepsilon > 4$, the texture evolution suggests that GBS is an extensively operating deformation mechanism. It has been shown that 1421 Al with an average grain size of ~1 μm exhibits moderate superplastic properties at 300 °C and $\dot{\varepsilon} = 10^{-1}$ s^{-1} [3], which supports this conclusion. Therefore, GBS can occur in 1421 Al during ECAE in the partially recrystallized structure with an average size of crystallites of about 1 μm thus promoting the transformation of LABs into HABs (Fig. 7d). Superposition of trapping lattice dislocation by immobile sub-boundaries and (sub)grain rotation due to GBS along isolated segments of deformation-induced boundaries with a high-angle mis-orientation provides a very high rate of conversion from LABs to HABs with strain.

Thus, extensive grain refinement in 1421 Al resulting in a reduction in grain size from ~60 μm to ~0.9 μm at an intermediate temperature 300 °C under ECAE is attributed to the occurrence of continuous dynamic recrystallization. The chemical and phase composition of 1421 Al facilitates this process.

5. Conclusions

Equal-channel angular extrusion of a commercial Al–Li–Mg–Sc alloy at 300 °C with a total strain of 12 provides the formation of a fully recrystallized equilibrium structure with an average grain size ~0.9 μm containing a relatively low density of dislocations.

The microstructural evolution during equal-channel angular extrusion occurs through continuous dynamic recrystallization. After the first passage through the die ($\varepsilon \sim 1$), arrays of low-angle boundaries evolve. Further deformation leads to the gradual transformation of low-angle boundaries into high angle boundaries at a high rate. New grains evolve homogeneously both within interiors of initial grains and along old boundaries as well.

The rate of increasing average mis-orientation with strain ($\Delta\theta \propto 5^\circ \times \varepsilon$) is high. The mis-orientation of deformation-induced boundaries approaches the theoretical limit for a random distribution of polycrystalline grains at $\varepsilon \sim 8$. The size of deformation-induced (sub)grains remains essentially unchanged during intense plastic deformation due to the presence of coherent dispersoids.

Acknowledgements

This work was supported in part by the International Science and Technology Center under Project no.2011 and the Japan Light Metal Educational Foundation.

References

[1] I.N. Fridlyander, K.V. Chuistova, A.L. Berezina, N.I. Kolobnev, Aluminum–Lithium alloys: Structure and Properties, Naukova Dumka, Kiev, 1992, pp. 155–176.
[2] S. Lee, P. Berbon, M. Furukawa, Z. Horita, M. Nemoto, N. Tsenev, R. Valiev, T.G. Langdon, Mater. Sci. Eng. A 272 (1999) 63.
[3] R. Kaibyshev, F. Musin, Y. Motohashi, Mater. Trans. 43 (2002) 2370.
[4] A. Golinia, P.B. Prangnell, M.V. Markushev, Acta Mater. 48 (2000) 1115.
[5] S. Ferrase, V. Segal, K. Hartwig, R. Goforth, Metall. Mater. Trans 28A (1997) 1047.
[6] Y. Iwahashi, Z. Horita, M. Nemoto, T.G. Langdon, Acta Mater. 46 (1998) 3317.
[7] Y. Iwahashi, Z. Horita, M. Nemoto, T.G. Langdon, Acta Mater. 45 (1997) 4733.
[8] K. Nakashima, Z. Horita, M. Nemoto, T.G. Langdon, Acta Mater. 46 (1998) 1589.
[9] F.J. Humphreys, P.B. Prangnell, J.R. Bowen, A. Gholinia, C. Harris, Phil. Trans. R. Soc. Lond. 357A (1999) 1663.
[10] P.J. Apps, J.R. Bowen, P.B. Prangnell, Acta Mater. 51 (2003) 2811.
[11] W.Q. Cao, A. Godfrey, Q. Liu, Mater. Sci. Eng. 361 (2003) 9.
[12] S.D. Terhune, D.L. Swisher, K. Oh-ishi, Z. Horita, T.G. Langdon, T.R. McNelley, Metall. Mater. Trans. 33A (2002) 2173.
[13] C.P. Chang, P.L. Sun, P.W. Kao, Acta Mater. 48 (2000) 3377.
[14] F.J. Humphreys, M. Hatherly, Recrystallization and Related Annealing Phenomena, Pergamon Press, Oxford, UK, 1996.
[15] S. Courdet, F. Montheillet, Acta Mater. 51 (2003) 2685.
[16] Z. Horita, M. Furukawa, M. Nemoto, T.G. Langdon, Mater. Sci. Technol. 16 (2000) 1239.
[17] I.J. Beyerlein, N. Carlos, Tome, Mater. Sci. Eng. A 380 (2004) 171.
[18] S.L. Semiatin, D.P. Delo, E.B. Shell, Acta Mater. 48 (2000) 1841.
[19] S.C. Baik, Yu. Estrin, H.S. Kim, R.J. Hellmig, Mater. Sci. Eng. A351 (2003) 86.
[20] H. Jazaeri, F.J. Humphreys, Acta Mater. 52 (2004) 3239.
[21] P.B. Hirsh, A. Howie, R.B. Nicholson, D.W. Pashley, M.J. Whelan, Electron Microscopy of Thin Crystals, Butterworths, London, 1965.
[22] R. Kaibyshev, F. Musin, D. Gromov, T.G. Nieh, D.R. Lesuer, Mater. Sci. Technol. 19 (2003) 483.
[23] R. Kaibyshev, F. Musin, K. Saytaeva, Y. Motohashi, in: Y.T. Zhu, T.G. Langdon, M.J. Saran, T.C. Lowe (Eds.), Ultrafine Grained Materials II, TMS, 2002, p. 81.
[24] Q. Liu, X. Huang, M. Yao, J. Yang, Acta Metal. Mater. 40 (1992) 1753.
[25] A. Belyakov, T. Sakai, H. Miura, K. Tsuzaki, Phil. Mag. A 81 (2001) 2629.
[26] J.K. Mackenzie, Biometrika 45 (1958) 229.
[27] A. Gholinia, F.J. Humphreys, P.B. Prangnell, Acta Mater. 50 (2002) 4461.
[28] MR. Barnett, F. Montheillet, Acta Mater. 50 (2002) 2285.
[29] F. Montheillet, M. Cohen, J. Jonas, Acta Metall. 32 (1984) 2077.
[30] P.B. Prangnell, J.S. Hayes, J.R. Bowen, P.J. Apps, P.S. Bate, Acta Mater. 52 (2004) 3193.
[31] J.R. Bowen, A. Gholinia, S.M. Roberts, P.B. Prangnell, Mater. Sci. Eng. A 287 (2000) 87.
[32] S. Gourdet, F. Montheillet, Mater. Sci. Eng. A 283 (2000) 274.
[33] M. Biberger, W. Blum, Phil. Mag. A 65 (1992) 757.
[34] O. Sitdikov, R. Kaibyshev, Mater. Sci. Eng. 334 (2002) 104.
[35] L.M. Dougherty, I.M. Robertson, J.S. Vetrano, Acta Mater. 51 (2003) 4367.
[36] Y. Fukuda, K. Oh-ishi, M. Furukawa, Z. Horita, T.G. Langdon, Acta Mater. 52 (2004) 1387.
[37] L.P. Troeger, E.A. Starke Jr., Mater. Sci. Eng. A 277 (2000) 102.
[38] F.J. Humphreys, Mater. Sci. Forum 447–448 (2003) 107.
[39] S.J. Hales, T.R. McNelley, H.J. McQueen, Metall. Trans. A 22 (1991) 1037.
[40] R. Kaibyshev, A. Goloborodko, F. Musin, I. Nikulin, T. Sakai, Mater. Trans. 43 (2002) 2408.
[41] X. Yang, H. Miura, T. Sakai, Mater. Trans. 43 (2002) 2400.